

Higher-order skyrmion crystal in van der Waals Kitaev triangular antiferromagnet NiI_2

Chaebin Kim^{1,2,3*}, Olivia Vilella^{3*}, Youjin Lee^{1,2*}, Pyeongjae Park^{1,2}, Yeochan An^{1,2}, Woonghee Cho^{1,2}, Matthew B. Stone⁴, Alexander I. Kolesnikov⁴, Shinichiro Asai⁵, Shinichi Itoh⁶, Takatsugu Masuda⁵, Sakib Matin^{7,8}, Sujin Kim⁹, Sung-Jin Kim⁹, Martin Mourigal^{3#} and Je-Geun Park^{1,2#}

¹Center for Quantum Materials, Seoul National University; Seoul 08826, Republic of Korea

²Department of Physics and Astronomy, Seoul National University; Seoul 08826, Republic of Korea

³School of Physics, Georgia Institute of Technology; Atlanta, Georgia 30332, USA

⁴Neutron Scattering Division, Oak Ridge National Laboratory; Oak Ridge, Tennessee 37831, USA

⁵Institute for Solid State Physics, The University of Tokyo; Chiba 277-8581, Japan

⁶Institute of Materials Structure Science, High Energy Accelerator Research Organization; Tsukuba 305-0801, Japan

⁷Center for Nonlinear Studies, Los Alamos National Laboratory, Los Alamos, NM, 87545, USA

⁸Theoretical Division, Los Alamos National Laboratory, Los Alamos, NM, 87545, USA

⁹Department of Chemistry and Nano Science, Ewha Womans University; Seoul 03760, Republic of Korea

*Authors with equal contribution

#Corresponding Authors: mourigal@gatech.edu & jgpark10@snu.ac.kr

Abstract

Topological spin textures, such as magnetic skyrmions, hold great promise for spintronics applications. However, most known skyrmion systems are restricted to a topological charge of one and require an external magnetic field for stabilization. Here, we report the discovery of a skyrmion crystal with a topological number of two in an insulating van der Waals magnet NiI_2 . We unveil the static and dynamic magnetic correlations across three temperature-driven magnetic phases using neutron scattering measurements, simulations, and model optimisation. By employing a minimal Kitaev-Heisenberg Hamiltonian, we reproduce the experimentally observed excitations and confirm the emergence of the higher-order skyrmion crystal through Monte Carlo simulations. Remarkably, this exotic phase arises without the need for a magnetic field, presenting a novel platform for controlling complex spin textures in an accessible material. These findings establish NiI_2 as a pivotal material, bridging fundamental quantum magnetism with advancements in skyrmionics and multiferroic technologies.

Main text

Magnetic skyrmions, topological solitons defined by the winding number of their spin texture [1-2], have emerged as a promising platform for spintronics applications [3]. Since the discovery of a skyrmion crystal – a phase marked by the periodic arrangement of magnetic skyrmions – in metallic MnSi under an applied magnetic field [4-5], numerous realizations of skyrmions have been reported. However, in all known materials [2,6], the topological number (or topological charge) N_{sk} of these solitons is limited to one (skyrmions) or one-half (merons) [2,7]. While higher-order skyrmion crystals with $N_{\text{sk}} > 1$ are theoretically possible [8], they remain experimentally elusive. These periodic higher-order skyrmion phases, characterized by extreme spin noncoplanarity, are particularly appealing for spintronics due to their predicted unconventional transport phenomena and the potential for topological charge control via external perturbations [7-8].

Two distinct mechanisms are known to stabilize $N_{\text{sk}} = 1$ skyrmion crystal phases: the Dzyaloshinskii-Moriya (DM) interaction in non-centrosymmetric systems or the Ruderman-Kittel-Kasuya-Yoshida (RKKY) interaction in metallic systems [9]. However, both mechanisms invariably require an external magnetic field for stabilization. Theoretical studies, however, propose that higher-order skyrmion crystal phases, such as the $N_{\text{sk}} = 2$ (SkX-2) phase, can be achieved through alternative mechanisms [7,9]. One such mechanism involves the Kitaev exchange interaction [8], where bond-directional Ising-like interactions stabilize the SkX-2 phase in a thermal equilibrium state without the need for a magnetic field. Despite this theoretical potential, the experimental realization of the SkX-2 phase has remained elusive in a bulk material- until now. In this work, we identify the van der Waals (vdW) multiferroic antiferromagnet NiI_2 as a promising candidate for realizing the SkX-2 phase.

NiI_2 belongs to a large family of vdW transition-metal dihalides (see Fig.1(a) for the crystal structure) known for their rich magnetic properties [10-14], including multipolar excitations [15] and Kitaev exchange interactions enhanced by the spin-orbit coupling at iodine ligands [16]. Unique among this family, NiI_2 exhibits a stable multiferroic phase that extends to the bilayer [12] and monolayer limits [14]. In bulk form, NiI_2 undergoes two successive magnetic phase transitions at $T_{\text{N1}} = 75$ K and $T_{\text{N2}} = 60$ K, as shown by susceptibility measurements (Fig.1(b)) and temperature-dependent elastic neutron scattering patterns (Fig.1(c)), which also depict the associated magnetic structures. The multiferroic phase below T_{N2} features an incommensurate helical magnetic structure (MF-Helix) with the propagation vector $\mathbf{Q}_{\text{m2}} = (0.1384, 0, 1.457)$ [11], electric polarisation \mathbf{P} along the (1, 1, 0) direction, and a strong optical second harmonic generation (SHG) signal [12,14].

In contrast, the true nature of the intermediate phase between T_{N1} and T_{N2} remains poorly understood, with prior studies offering only an untested hypothesis of a collinear magnetic structure. This phase exhibits a commensurate out-of-plane magnetic structure with a propagation vector $\mathbf{Q}_{\text{m1}} = (0.083, 0.083, 1.5)$ and no SHG signal, indicating preserved inversion symmetry and a possible collinear antiferromagnetic structure [12,14]. However, first-principles calculations for NiI_2 suggest significant Kitaev and frustrated further-neighbour exchange interactions, predicted to stabilize a SkX-2 phase in the monolayer limit [8,17-18]. These findings motivate a comprehensive experimental investigation of the intermediate phase in bulk NiI_2 to determine whether it hosts the elusive SkX-2 phase.

In this study, we employ elastic and inelastic neutron scattering, combined with semi-classical spin dynamics simulations and inverse modelling techniques, to refine the model Hamiltonian of bulk NiI_2 . Our investigation begins with the spin excitations in the correlated paramagnet (PM) just above T_{N1} , where spin correlations reveal direct evidence of antiferromagnetic Kitaev interactions. Extending our analysis to the intermediate (IN) and multiferroic (MF) phases, we quantify the relevant energy scales and develop a comprehensive understanding of the material's exchange Hamiltonian.

Using this refined model, Monte Carlo and Landau-Lifshitz simulations accurately reproduce the experimentally observed static and dynamic spin correlations in the intermediate phase between T_{N1} and T_{N2} . These simulations also predict the presence of a SkX-2 magnetic ground state, a high-order skyrmion crystal with a topological charge of two. Remarkably, this phase is consistent with earlier optical experiments. Our combined experimental and theoretical approaches strongly support the existence of a high-topological-number skyrmion crystal phase at an intermediate temperature in NiI_2 .

We begin by defining a minimal bilinear magnetic Hamiltonian for NiI_2 , constrained by the symmetry of the paramagnetic $R\bar{3}m$ space group. This symmetry allows for bond-dependent anisotropic exchange interactions. First-principle calculations [8,17-18] indicate that Heisenberg and Kitaev interactions dominate on nearest-neighbour bonds. Therefore, our analysis focuses on these terms, incorporating further-neighbour interactions as required. Given that second-nearest-neighbour intralayer coupling J_2 is negligible in most Ni-based compounds with edge-sharing octahedral networks, we omit this term from our model [19-20]. The resulting Hamiltonian, expressed with four independent parameters, is:

$$H = \sum_{\langle i,j \rangle_1 \in \{\alpha, \beta, \gamma\}} \{J_1 \mathbf{S}_i \cdot \mathbf{S}_j + K S_i^x S_j^x\} + \sum_{\langle i,j \rangle_n}^{3, c_1, c_2} J_n \mathbf{S}_i \cdot \mathbf{S}_j \quad (1)$$

where $n = 1, 3$ indicates the intralayer n -th nearest neighbour, $n = c_1, c_2$ indicates the interlayer n -th nearest neighbour coupling, and K represents the Kitaev interaction for X -, Y -, and Z -bond (see Fig. S1 for definitions [21]).

To gain deeper insight into the microscopic exchange interactions, we analyze the paramagnetic regime of NiI_2 just above T_{N1} . This regime provides a simplified setting for extracting model parameters, as thermal fluctuations dominate over quantum effects [22], eliminating the need for precise knowledge of spin waves. Additionally, the paramagnetic neutron scattering signal, sensitive to bond-dependent anisotropy, exhibits an out-of-plane intensity dependence due to the polarization factor of the neutron scattering cross-section [22].

Fig. 2(a) presents the dependence of the paramagnetic signal on momentum transfer \mathbf{Q} and energy transfer E at $T = 100$ K along several high-symmetry paths in reciprocal space $\mathbf{Q} = (H, K, L^*)$ for $L^* = 0$ and $L^* = 1.5$ (see Fig. S3 for path definitions in the hexagonal Brillouin zone [21]). The neutron scattering intensity is concentrated close to Brillouin zone centers, reflecting the long real-space length associated with $2\pi/|\mathbf{Q}_m|$. In addition, Fig. 2(b)-(e) shows the energy-integrated ($E = [1, 6]$ meV) paramagnetic signal (diffuse scattering) in two momentum-space planes; $\mathbf{Q} = (H, K, L^*)$ with fixed $L^* = 0, \pm 1.5$, and $\mathbf{Q} = (H, 0, L)$. For $L^* = 0$, we observe hexagonally-shaped diffuse scattering at low- \mathbf{Q} and near zone centers (Fig. 2(b)).

When $L^* = \pm 1.5$, the 6-fold intensity reduces to threefold, with its orientation depending on the sign of L^* (see Fig. S4 [21]). In our model, this L -dependent behaviour of the diffuse scattering uniquely signals the presence of a Kitaev interaction [22].

Next, we calculate the neutron scattering intensity at finite temperatures using Landau-Lifshitz dynamics (LLD) simulations [23] based on the refined Hamiltonian from Eq. (1), constrained by the low-temperature magnetic structure. Bayesian optimization yields the best-fit parameters as $J_1 = -7.4(1)$ meV, $K = 2.5(5)$ meV, $J_3 = 2.7(1)$ meV, and $J_{c2} = 1.24(5)$ meV (See supplementary materials and Fig. S6 for details [21]). LLD calculations with these parameters agree closely with experimental data at $T = 100$ K, as shown on the right side of Fig. 2(a) and Fig. 2(b)-(e). The calculated intensity patterns reproduce key features of the paramagnetic regime, confirming the model's validity at higher temperatures. Fig. 2(f) represents the excitations in the intermediate phase at $T = 70$ K, where our model successfully captures the V-shaped excitations near the zone centers. Additionally, constant energy slices at $T = 70$ K (Fig. 2(g)) reveal a two-peak structure consistent with coherent dispersing modes in the experimental data and simulations. These results further validate the refined Hamiltonian and its ability to accurately describe the intermediate phase's magnetic properties.

We now examine broadband measurements of the magnetic excitation spectrum in the MF-Helix phase at $T = 5$ K. As shown in Fig. 3(a), broad spin-wave-like excitations emerge from the \mathbf{Q}_{m2} points in reciprocal space, exhibiting a bandwidth that exceeds the $E = 20$ meV limit of our measurements, with a local maximum around $E = 8$ meV. The spin gap at the magnetic Bragg peak is measured to be less than 0.3 meV (see Fig. S7 [21]). Simulations of the MF-Helix phase were performed using the previously derived exchange parameters, with a slight deviation (1% of J_1) to the nearest-neighbour Heisenberg interaction. This small deviation accounts for the distorted triangular lattice and stabilizes the observed single- \mathbf{Q}_m magnetic order (see Fig. S1 [21]). Classical energy minimization followed by linear spin-wave theory (LSWT) produced simulations that align closely with the experimental results, including constant-energy slices, without requiring further tuning of the exchange interactions (see Fig. 3(b)-(e)).

Taken together, our investigations establish a minimal exchange Hamiltonian that accurately reproduces the elastic, diffuse, and inelastic neutron scattering responses of NiI_2 across three distinct thermodynamic phases. We next focus on the precise nature of the intermediate phase between T_{N1} and T_{N2} . While neutron scattering averages over the entire sample, making it challenging to distinguish between a multi- \mathbf{Q}_m structure and domains of a single- \mathbf{Q}_m structure, Monte Carlo simulations using our refined model parameters and two different lattice symmetries provide critical insights [21] For the orthorhombic lattice structure associated with the multiferroic phase, the magnetic ground state corresponds to a spin helix with an in-plane propagation vector along the $(1,0,0)$ direction (see Fig. 4(a)). In contrast, the in-plane propagation vector shifts to $(1,1,0)$ for the hexagonal lattice structure while the spin texture becomes highly non-coplanar, signifying the stabilization of the SkX-2 phase in the simulations (Fig. 4(b)). This result highlights the critical interplay between lattice distortion, the multiferroic transition, and the change of magnetic structure.

To model the proposed SkX-2 phase, we employ a triple- \mathbf{Q}_m model, where each \mathbf{Q}_n is associated with a longitudinal spin-density-wave as follows [7]:

$$\mathbf{S}(\mathbf{r}_i) \cong \sum_{n=1}^3 A_n \hat{\mathbf{e}}_n \cos(\mathbf{Q}_n \cdot \mathbf{r}_i + \phi_n), \quad (2)$$

where $\mathbf{S}(\mathbf{r}_i)$ is the spin moment at position \mathbf{r}_i , and A_n is the contribution of each of three \mathbf{Q}_n , $\hat{\mathbf{e}}_n$ is a unit vector, ϕ_n is the phase factor associated with each of the propagation vectors $\mathbf{Q}_1 = (q_m, q_m, 1.5)$, $\mathbf{Q}_2 = (-2q_m, q_m, 1.5)$, $\mathbf{Q}_3 = (q_m, -2q_m, 1.5)$ with $q_m = 0.083$ fixed to the experimental value. Fitting this triple model to spin configurations from Monte Carlo simulations yields excellent agreement for $A_n = 0.7765$ for each n [21]. Under these conditions, the triple- \mathbf{Q}_m structure perfectly describes a SkX-2 crystalline phase with a high topological charge per soliton (see Fig. 4(c)).

Experimentally distinguishing between a single- \mathbf{Q}_m ordered structure with three domains and a single-domain triple- \mathbf{Q}_m structure is inherently challenging. Frustrated multiferroic compounds often exhibit sequential single- \mathbf{Q}_m spin-density-wave orderings [24], typically stabilized by uniaxial easy-axis anisotropy favouring a single- \mathbf{Q}_m state. However, NiI_2 deviates from this norm. Unlike other multiferroic compounds, it lacks significant uniaxial anisotropy. Instead, the Kitaev interaction stabilizes three mutually orthogonal spin-density-wave-like modes, making the single- \mathbf{Q}_m spin-density-wave phase energetically unfavourable in our hexagonal model of NiI_2 . Given these considerations, interpreting the intermediate phase as the SkX-2 phase is the most reasonable explanation.

The superposition of three spin-density-wave modes preserves inversion symmetry, consistent with the absence of SHG or ferroelectricity observed experimentally in the proposed SkX-2 phase [13]. However, bulk NiI_2 display weak linear optical dichroism below T_{N1} [14], suggesting a potential breaking in the threefold rotational symmetry of the paramagnetic lattice. This dichroism could result from an unequal distribution of three single- \mathbf{Q}_m spin-density-wave domains across the sample or from a distorted triple- \mathbf{Q}_m SkX-2 phase with imbalanced A_n amplitudes. Such imbalances may arise due to the thermal fluctuations or subleading terms in the Hamiltonian. While distinguishing these scenarios requires further investigation, the optical measurements strongly support the conclusion that the sizable Kitaev interaction in NiI_2 stabilizes an exotic phase between T_{N1} and T_{N2} . This finding advances our understanding of the material's complex magnetic behavior [12,14].

In conclusion, NiI_2 emerges as a unique quantum material that bridges the fundamental physics of Kitaev quantum magnetism with applications in two-dimensional thin-layer multiferroicity. We identify a significant Kitaev interaction in this van der Waals triangular-lattice antiferromagnet through neutron scattering and semi-classical modelling. This interaction, together with four additional exchange parameters, defines a minimal model that accurately describes the static and dynamical magnetic properties across three distinct thermodynamics phases: a cooperative paramagnet above 75 K, an intermediate phase between 60 and 75 K, and a multiferroic helicoidal phase below 60 K. Monte Carlo simulations of the refined model reveal the likely stabilization of an intermediate triple- \mathbf{Q}_m structure, corresponding to a higher-order SkX-2 skyrmion crystal. This exotic phase, characterized as a coherent superposition of three orthogonally polarised spin-density wave modes, is a direct consequence of the strong Kitaev interaction. Unlike conventional skyrmion mechanisms that rely on RKKY and Dzaloshinskii-Moriya interactions, the SkX-2 phase in NiI_2 arises independently of such effects, underscoring its novel magnetic behavior.

Acknowledgments

The authors thank Cristian Batista and Jong-Seok Lee for their fruitful discussion and constructive comments. The authors also thank Maxim Avdeev for his help with powder neutron diffraction measurement. The work at SNU was supported by the Leading Researcher Program of the National Research Foundation of Korea (Grant No. 2020R1A3B2079357) and the National Research Foundation of Korea (Grant No RS-2020-NR049405). The work of O.V. and M.M was supported by the U.S. National Science Foundation through Grant No. NSF-DMR-1750186. S. Matin acknowledges support from the Center for Nonlinear Studies at Los Alamos National Laboratory. The work of S.K. and S.J.K. was supported by the Pioneer Research Center Program through the National Research Foundation of Korea, funded by the Ministry of Science, ICT & Future Planning (NRF-2022M3C1A3091988). Part of this research was conducted at the Spallation Neutron Source, a DOE Office of Science User Facility operated by the Oak Ridge National Laboratory. Another neutron experiment was performed at the Materials and Life Science Experimental Facility of the J-PARC Center under a user program 2022BU1201. One of the authors (J.G.P.) acknowledges the hospitality of the Indian Institute of Science, where the manuscript was finalised, and the financial support of the Infosys Foundation.

References

- [1] A. Fert, N. Reyren, and V. Cros, Magnetic skyrmions: advances in physics and potential applications. *Nat Rev Mater* **2**, 17031 (2017).
- [2] N. Nagaosa and Y. Tokura, Topological properties and dynamics of magnetic skyrmions. *Nat Nanotechnol* **8**, 899–911 (2013).
- [3] S. Parkin, and S. -H. Yang, Memory on the racetrack. *Nat Nanotechnol* **10**, 195–198 (2015).
- [4] S. Mühlbauer, *et al.* Skyrmion Lattice in a Chiral Magnet. *Science* (1979) **323**, 915–919 (2009).
- [5] U. K. Rößler, A. N. Bogdanov, and C. Pfleiderer, Spontaneous skyrmion ground states in magnetic metals. *Nature* **442**, 797–801 (2006).
- [6] S. Gao, H. Rosales, F. A. Gomez, V. Tsurkan, G. Kaur, T. Fennell, P. Steffens, M. Boehm, P. Cermak, A. Schneidewind, E. Ressouche, D. Cabra, C. Ruegg, O. Zahrko, Fractional antiferromagnetic skyrmion lattice induced by anisotropic couplings. *Nature* **586**, 37–41 (2020).
- [7] R. Ozawa, S. Hayami, and Y. Motome, Zero-Field Skyrmions with a High Topological Number in Itinerant Magnets. *Phys Rev Lett* **118**, 147205 (2017).
- [8] D. Amoroso, P. Barone, and S. Picozzi, Spontaneous skyrmionic lattice from anisotropic symmetric exchange in a Ni-halide monolayer. *Nat Commun* **11**, 5784 (2020).
- [9] C. D. Batista, S. -Z. Lin, S. Hayami, and Y. Kamiya, Frustration and chiral orderings in correlated electron systems. *Reports on Progress in Physics* **79**, 084504 (2016).
- [10] M. McGuire, Crystal and Magnetic Structures in Layered, Transition Metal Dihalides and Trihalides. *Crystals (Basel)* **7**, 121 (2017).
- [11] S. R. Kuindersma, J. P. Sanchez, and C. Haas, Magnetic and structural investigations on NiI_2 and CoI_2 . *Physica B+C* **111**, 231–248 (1981).
- [12] H. Ju, Y. Lee, K. -T. Kim, I. Choi, C. Roh, S. Son, P. Park, J. Kim, T. S. Jung, J. H. Kim, K. H. Lee, J. -G. Park, J. S. Lee, Possible Persistence of Multiferroic Order down to Bilayer Limit of van der Waals Material NiI_2 . *Nano Lett* **21**, 5126–5132 (2021).
- [13] T. Kurumaji, S. Seki, S. Ishiwata, H. Murakawa, Y. Kaneko, Y. Tokura, Magnetoelectric responses induced by domain rearrangement and spin structural change in triangular-lattice helimagnets NiI_2 and CoI_2 . *Phys Rev B* **87**, 014429 (2013).
- [14] Q. Song, C. A. Occhialini, E. Ergecen, B. Ilyas, D. Amoroso, P. Barone, J. Kapeghian, K. Watanabe, T. Taniguchi, A. S. Botana, S. Picozzi, N. Gedik, R. Comin, Evidence for a single-layer van der Waals multiferroic. *Nature* **602**, 601–605 (2022).
- [15] X. Bai, S. S. Zhang, H. Zhang, Q. Huang, H. Zhou, M. B. Stone, A. I. Kolesnikov, F. Ye, C.D. Batista, M. Mourigal, Hybridized quadrupolar excitations in the spin-anisotropic frustrated magnet FeI_2 . *Nat Phys* **17**, 467–472 (2021).
- [16] C. Kim, S. Kim, P. Park, T. Kim, J. Jeong, S. Ohira-Kawamura, N. Murai, K. Nakajima, A. L. Chernyshev, M. Mourigal, S. -J. Kim, J. -G. Park, Bond-dependent anisotropy and magnon decay in cobalt-based Kitaev triangular antiferromagnet. *Nat Phys* **19**, 1624–1629 (2023).
- [17] P. P. Stavropoulos, D. Pereira, and H. -Y. Kee, Microscopic Mechanism for a Higher-Spin Kitaev Model. *Phys Rev Lett* **123**, 037203 (2019).
- [18] X. Li, C. Xu, L. B. Liu, X. Li, L. Bellaiche, H. Xiang, Realistic Spin Model for Multiferroic NiI_2 . *Phys Rev Lett* **131**, 036701 (2023).

- [19] A. Scheie, P. Park, J. W. Villanova, G. E. Granroth, C. Sarkis, H. Zhang, M. B. Stone, J. -G. Park, S. Okamoto, T. Berlijn, D. A. Tennant, Spin wave Hamiltonian and anomalous scattering in NiPS₃. *Phys Rev B* **108**, 104402 (2023).
- [20] C. Stock, S. Jonas, C. Broholm, S. Nakatsuji, Y. Nambu, K. Onuma, Y. Maeno, J. -H. Chung, Neutron-Scattering Measurement of Incommensurate Short-Range Order in Single Crystals of the S=1 Triangular Antiferromagnet NiGa₂S₄. *Phys Rev Lett* **105**, 037402 (2010).
- [21] See Supplementary Material for crystal synthesis, neutron scattering experiments, LLD and LSWT simulations, classical energy minimization, fitting details, and the transformation between the cubic axis and crystallographic axis, which includes Refs. [25-34].
- [22] J. A. M. Paddison, Scattering Signatures of Bond-Dependent Magnetic Interactions. *Phys Rev Lett* **125**, 247202 (2020).
- [23] D. Dahlbom, H. Zhang, C. Miles, X. Bai, C. D. Batista, K. Barros, Geometric integration of classical spin dynamics via a mean-field Schrödinger equation. *Phys Rev B* **106**, 054423 (2022).
- [24] S. -W. Cheong, & M. Mostovoy, Multiferroics: a magnetic twist for ferroelectricity. *Nat Mater* **6**, 13–20 (2007).
- [25] G. E. Granroth, A. I. Kolesnikov, T. E. Sherline, J. P. Clancy, K. A. Ross, J. P. C. Ruff, C. D. Gaulin, S. E. Nagler, SEQUOIA: A Newly Operating Chopper Spectrometer at the SNS. *J Phys Conf Ser* **251**, 012058 (2010).
- [26] O. Arnold, J. C. Bilheux, J.M. Borreguero, A. Buts, S. I. Campbell, L. Chapon, M. Doucet, N. Draper, R. Ferra Leal, M. A. Gigg, V. E. Lynch, A. Markvardsen, D. J. Mikkelsen, R. L. Mikkelsen, R. Miller, K. Palmen, P. Parker, G. Passos, T. G. Perring, P. F. Peterson, S. Ren, M. A. Reuter, A. T. Savici, J. W. Taylor, R. J. Taylor, R. Tolchenov, W. Zhou, J. Zikovsky, Mantid—Data analysis and visualization package for neutron scattering and μ SR experiments. *Nucl Instrum Methods Phys Res A* **764**, 156–166 (2014).
- [27] R. A. Ewings, A. Buts, M. D. Le, J. van Duijn, I. Bustinduy, T. G. Perring, Horace : Software for the analysis of data from single crystal spectroscopy experiments at time-of-flight neutron instruments. *Nucl Instrum Methods Phys Res A* **834**, 132–142 (2016).
- [28] S. Itoh, T. Yokoo, S. Satoh, S. Yano, D. Kawana, J. Suzuki, T. J. Sato, High Resolution Chopper Spectrometer (HRC) at J-PARC. *Nucl Instrum Methods Phys Res A* **631**, 90–97 (2011).
- [29] Sunny. <https://github.com/Sunnysuite/Sunny>.
- [30] L. Harry, H. Zhang, D. Dahlbom, S. Quinn, R. D. Somma, M. Mourigal, C. D. Batista, K. Barros, Kernel polynomial method for linear spin wave theory. *SciPost Phys* **17**, 145 (2024)
- [31] D. B. Litvin, The Luttinger-Tisza method. *Physica* **77**, 205–219 (1974).
- [32] F. Nogueira, <https://github.com/fmfn/BayesianOptimization>. (2014).
- [33] Th. Proffen and T. R. Welberry, Analysis of Diffuse Scattering via the Reverse Monte Carlo Technique: a Systematic Investigation. *Acta Crystallogr A* **53**, 202–216 (1997).
- [34] P. A. Maksimov, Z. Zhu, S. R. White and A. L. Chernyshev, Anisotropic-Exchange Magnets on a Triangular Lattice: Spin Waves, Accidental Degeneracies, and Dual Spin Liquids. *Phys Rev X* **9**, 021017 (2019).

Figures

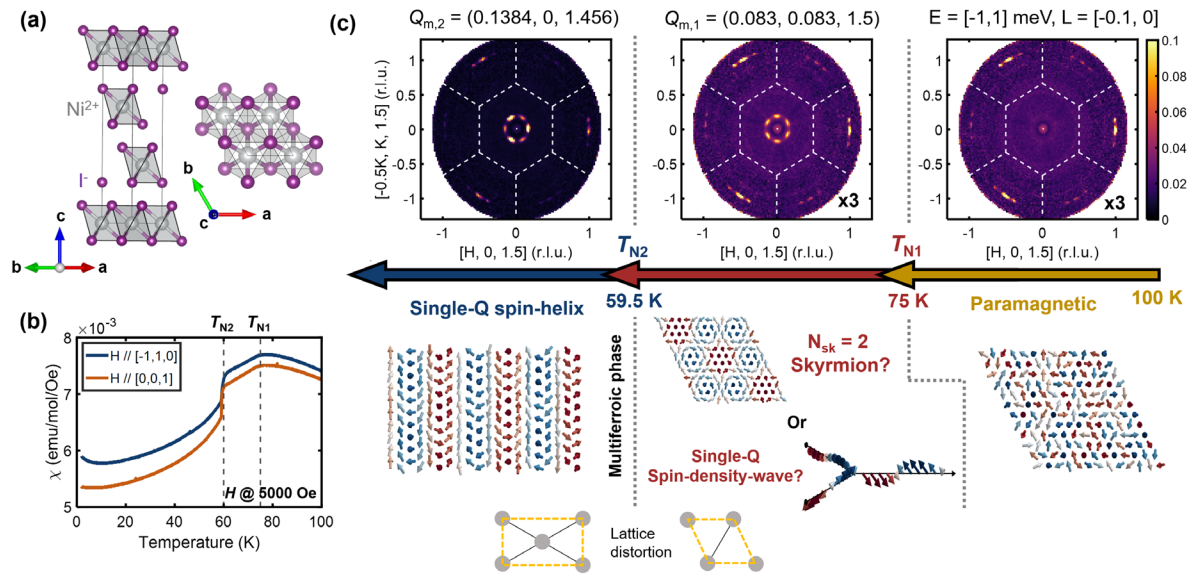


FIG. 1 Crystal structure and magnetic phases in NiI₂

(a) Crystal structure of NiI₂ in $R\bar{3}m$. The grey spheres represent Ni²⁺ ions, and the purple spheres represent Iodine ions. **(b)** Magnetic susceptibility of single crystal NiI₂ measured with different directions under a magnetic field $H = 0.5$ Tesla. The two grey lines serve as a guide to the eye, marking two magnetic phase transitions. **(c)** Schematic representation of magnetic phase transition in NiI₂. The upper panels show the magnetic Bragg peaks of NiI₂ at $T = 70$ K and $T = 4$ K. For elastic neutron scattering data, the integration range is $L = [-0.1, 0]$ and $E = [-1, 1]$ meV with an incident neutron energy of $E_i = 11.5$ meV. The lower panels depict cartoons of the possible magnetic structure in each magnetic phase. The arrow colour indicates the magnitude of the z-direction magnetic moment at each spin site (consistent with FIG. 4).

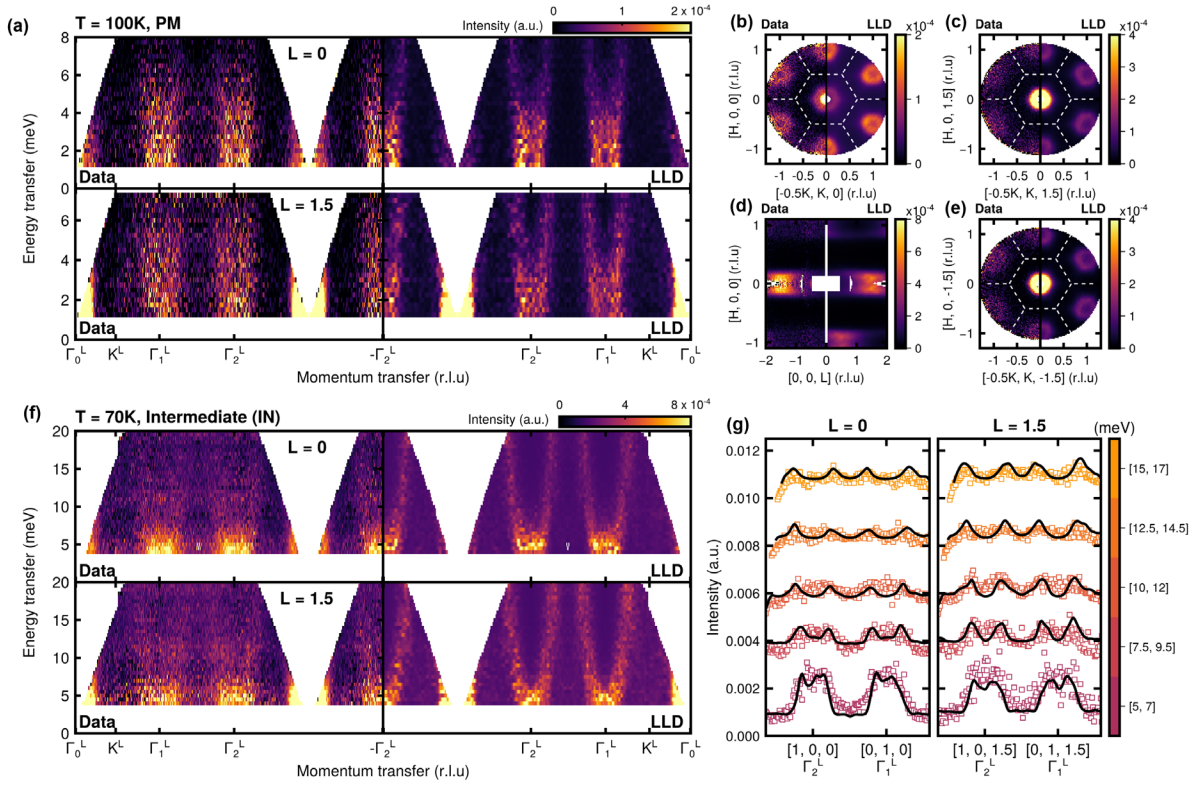


FIG 2. Energy-resolved paramagnetic and intermediate-phase excitations in NiI₂

(a) Energy-resolved neutron scattering intensity in the paramagnetic regime at $T = 100$ K along the symmetry directions of the hexagonal Brillouin zone with incident energy of $E_i = 11.5$ meV (see Fig. S2 for the directions [21]). The upper figure is for $L^* = 0$, and the bottom is for $L^* = 1.5$. The left side is the data, and the right side is the LLD simulation for our optimized exchange model. For the high symmetry points, $\Gamma_0^L = (0, 0, L^*)$, $\Gamma_1^L = (0, 1, L^*)$, $K^L = (1/3, 1/3, L^*)$, and $\Gamma_{\pm 2}^L = (\pm 1, 0, L^*)$. (b)-(e), Energy-integrated paramagnetic scattering intensity with $E = [1, 6]$ meV from the $E_i = 11.5$ meV data at $T = 100$ K. (b)-(c), (e) shows the (H, K, L^*) plane with $L^* = 0, 1.5, -1.5$, respectively. (d) shows the $(H, 0, L)$ plane. (f) Energy-resolved neutron-scattering intensity at $T = 70$ K with an incident energy of $E_i = 40$ meV. The upper figure is $L^* = 0$, and the bottom is $L^* = 1.5$. (g) shows the constant-energy cut of Fig. 2(f) near the two Gamma points, Γ_2^L and Γ_1^L with $L = 0$ and 1.5 at $T = 70$ K. The colour bar indicates the energy-integrated region of each constant-energy slice. Black lines show the LLD simulation with a given energy integration range.

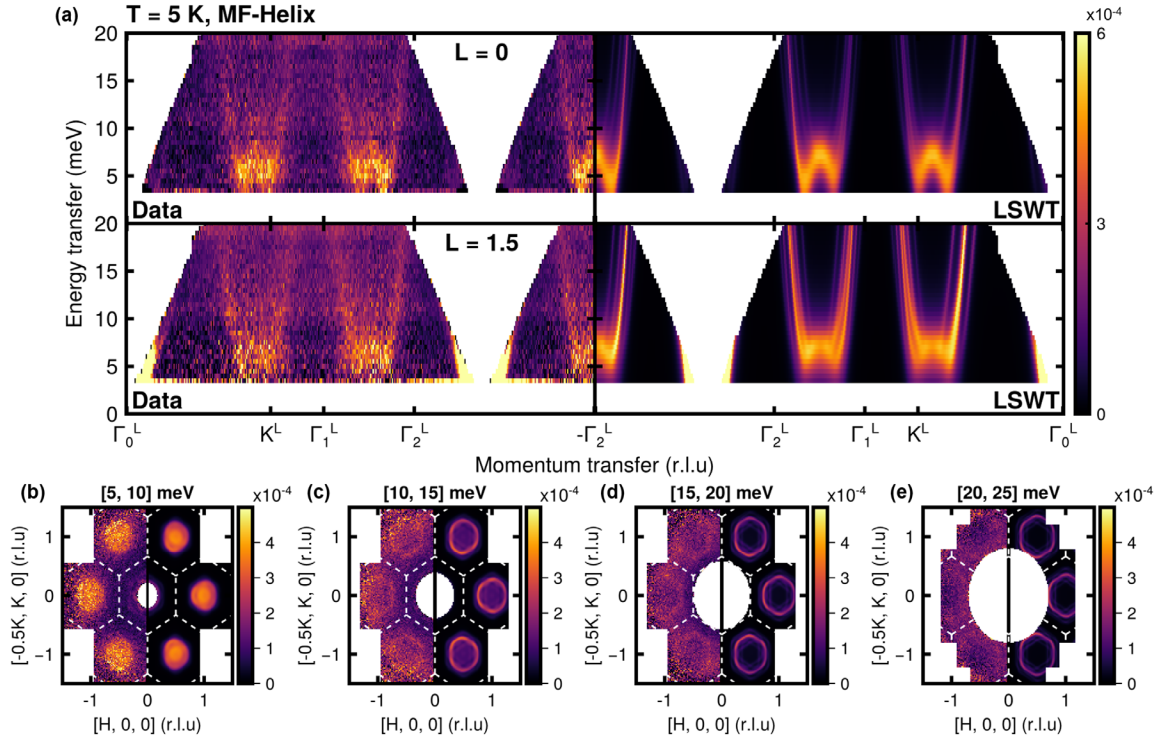


FIG 3. Spin-wave spectrum of in the low-temperature phase of Ni_2 .

(a) Spin-wave spectrum of the MF-Helix phase at $T = 5$ K with an incident energy of $E_i = 40$ meV. The upper panel show the $L^* = 0$ spectrum, and the bottom panel shows the spectrum at $L^* = 1.5$. The left panels display the experimental data, while the right panel presents simulations based on the linear spin-wave theory (LSWT) using the best-fit parameters for the PM phase. **(b)-(e)** Energy-integrated spin-wave spectrum at $L = [-0.25, 0.25]$. The integration range of energy for each figure is specified at the top of the respective panel. The left side of each panel shows experimental data and the right side shows the LSWT simulation. The colour bar represents the intensity of the dynamic structure factor of both data and simulations.

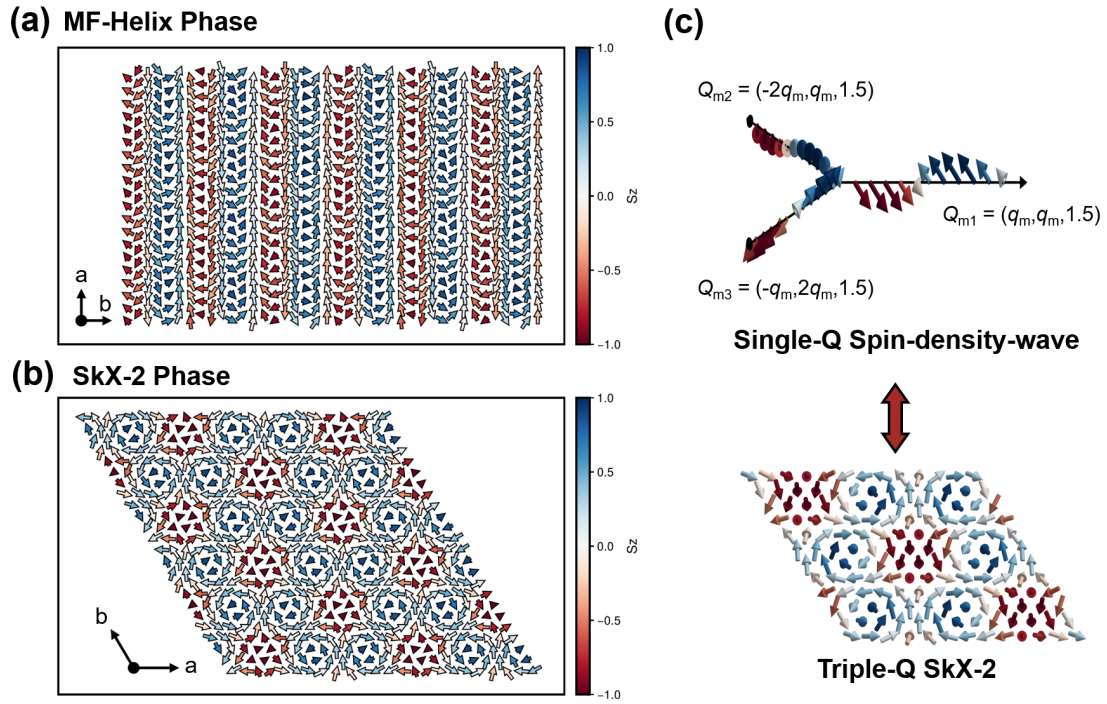


FIG 4. Lattice-symmetry dependent magnetic ground state in NiI_2 .

(a) Real-space spin configuration of the spiral phase obtained from the Monte Carlo simulation on an orthorhombic lattice. The colour bar indicates the z-direction spin moment. (b) Real-space spin configuration of the SkX-2 phase based on the MC simulation with a hexagonal lattice. (c) Schematic representation of the SkX-2 phase decomposed into three spin-density-wave phases.